RESEARCH ARTICLE

INTERNATIONAL RESEARCH JOURNAL OF MULTIDISCIPLINARY TECHNOVATION

Asian Research Association

DOI: 10.54392/irjmt25115

Synthesis and Electrochemical Characterization of TiO_2/g-C_3N_5 Coated 316L Stainless Steel for Orthopedic Applications

Padma Santhiya Muthu Krishnan [a], Manoja Tharmaraj [a], Abinaya Radhakrishnan [a], Anuradha Ramani [b], Nagarajan Srinivasan [a,*]

[a] Laboratory of Electrochemical Interfaces, Department of Chemistry, Manonmaniam Sundaranar University, Tirunelveli, Tamil Nadu, India.

[b] Department of Chemistry, Annai Hajira Women's College, Tirunelveli, Tamil Nadu, India.

* Corresponding Author Email: snagarajan@msuniv.ac.in

DOI: https://doi.org/10.54392/irjmt25115

Received: 13-11-2024; Revised: 11-01-2025; Accepted: 23-01-2025; Published: 30-01-2025

Abstract: This study investigates the effect of varying amounts of nitrogen-rich carbon nitride (g-C_3N_5) incorporated into titanium dioxide (TiO_2) coatings on 316L stainless steel (316LSS). The TiO_2/g-C_3N_5 coatings were tested in simulated body fluid (SBF) to assess their performance for orthopedic applications. TiO_2 was prepared using the sol-gel method, while g-C_3N_5 was synthesized through thermal polymerisation. The crystal structure, purity, and chemical composition of the TiO_2/g-C_3N_5 (TiCN) composites were confirmed using X-ray diffraction (XRD), Fourier transform infrared (FTIR) spectroscopy, and Raman analysis. The surface morphology of the coated samples was characterised using Scanning Electron Microscopy (SEM). In contrast, surface roughness was measured with Atomic Force Microscopy (AFM), revealing a porous film with an average particle size of 25 to 100 nm was coated over 316LSS. A fourfold increase in corrosion resistance was evaluated through Open circuit potential (OCP), Potentiodynamic polarisation, and Electrochemical impedance spectroscopy (EIS). The in vitro test revealed the enhanced growth of a hydroxyapatite layer on the coated TiCN. The elemental composition of calcium and phosphate ions present in the hydroxyapatite (HAP) deposition was confirmed using Raman spectroscopy. The results suggest that the TiCN coated 316LSS was a promising material for biomedical applications.

Keywords: Biomaterials, Corrosion, Graphitic carbon nitrite (g-C_3N_5), Titanium dioxide, Stimulated body fluid

1. Introduction

Metal implants are significant in biomedical applications due to their superior corrosion resistance and mechanical properties under physiological conditions [1, 2]. Surgical grade 316L stainless steel receives remarkable attention in the field of biomedical implants due to its corrosion resistance, affordability, manufacturability, longevity, and widespread availability [3]. The metallic ions like Ni_2+, Cr_3+, and Cr_6+ are released during the oxidisation and contribute to the loosening of prosthetic devices by having localised adverse effects on the implanted area [4, 5]. Corrosion prevention of 316LSS implants is important because it can adversely affect both the biocompatibility and mechanical strength of the implants. As a result, optimising the corrosion resistance and minimising ion release of 316LSS implants can be effectively achieved by surface modification with bioactive coatings, which promote cellular adhesion and bone integration [6]. To permanently protect its surfaces, an ideal biomaterial needs to have a robust framework with features like biocompatibility and improved corrosion resistance properties [7]. The use of various compounds enhances the biocompatibility and corrosion resistance. There have already been numerous attempts in this direction. Bioimplant materials have been subjected to coatings with a range of metal oxides, including TiO_2 [8, 9] ZrO_2 [10], SiO_2 [11], and Al_2O_3 [12]. Among these, titania (TiO_2) is used in the biomedical industry due to its high fracture resistance, durability, antibacterial activity and exceptional biocompatibility [13]. However, titanium dioxide (TiO_2) possesses certain inherent limitations, including poor mechanical properties of individual ceramic biomaterials that limit their performance in high load-bearing capacity [14]. Madan Kumar and Rajendran investigated the electrochemical and biological behavior of polypyrrole/titanium dioxide ceramic nanocomposite coatings on 316LSS and demonstrated that it is a promising material for orthopedic implants. These coatings reduce the corrosion rate and facilitate enhanced cell adhesion and proliferation [15]. K.T. Oh and Y. S. Park demonstrated that super austenitic stainless steel (SASS) coated with hydroxyapatite (HA) by plasma spraying provides excellent corrosion resistance and mechanical properties [16].

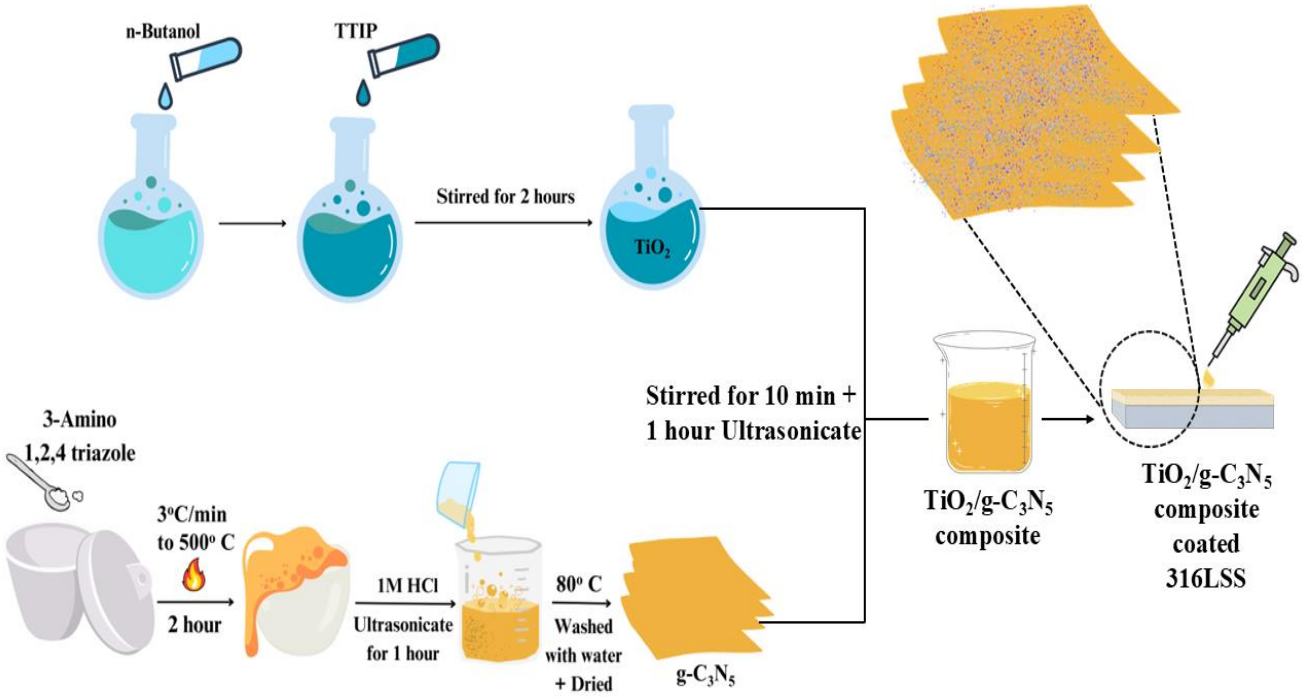

Figure 1. Schematic illustration for the formation of TiO_2/g-C_3N_5 Composites coating

Dai *et al.* reported that Al_2O_3-TiO_2 coatings with 15.56% titanium content visibly improved the corrosion resistance of 316LSS in chloride environments [17]. Garrido *et al.* showed that incorporating bioactive glass 45S5 with PEEK through cold gas spray improved the wear resistance and the integration between bone tissue and implant material [18]. TiO_2-based coatings for biomedical implants emphasize their corrosion resistance, biocompatibility, and potential for surface modification to enhance performance. However, the limitations of pure TiO_2, such as suboptimal mechanical stability and susceptibility to long-term degradation, highlight the need for composite materials. Therefore, to overcome these challenges, a well-established approach involves the preparation of nanocomposite coatings, which offer superior corrosion resistance compared to single-layer coatings. The success of an implant depends on the stability of its coating, which provides good biocompatibility. Using nanocomposites for surface modification is an effective strategy to improve implant performance [19-30].

g-C_3N_5, a graphitic carbon nitride material, has garnered attention in various fields, including photocatalysis, energy storage, and environmental remediation, due to its exceptional stability, chemical inertness, and tunable electronic properties. Its unique structure and synergistic potential when combined with other materials, such as TiO_2, have been shown to enhance photocatalytic activity and mechanical properties. However, its application in biomedical coatings, particularly for improving corrosion resistance and biocompatibility in implantable devices, remains unexplored. Adding polymeric mesoporous graphitic carbon nitride (g-C_3N_5) has garnered significant attention among the various methods for improving titania. g-C_3N_5 was chosen for its exceptional biocompatibility, high surface area, ordered porosity, stable chemical characteristics, biological activity and corrosion resistance. g-C_3N_5 offers a high nitrogen content and demonstrates remarkable properties across a wide range of applications 31-36. g-C_3N_5 is a new material, and there is limited review papers focus on understanding the photocatalytic applications of g-C_3N_5 compared to the g-C_3N_4. To date, no research has been done on the use of g-C_3N_5 in orthopedic applications. This highlights the need to explore its potential in this area, where its properties could offer new possibilities [37, 38]. As a result, g-C_3N_5 was successfully incorporated into TiO_2 for further investigation. There is no previous report of utilising 316LSS alloy coated with titanium dioxide and nitrogen-rich graphitic carbon nitride for biomedical applications. This study provides precise insights into the electrochemical behavior of materials and valuable information for developing effective corrosion-resistant coatings. Notably, applying substantial TiO_2/g-C_3N_5 coatings leads to marked improvements, enhancing biocompatibility and corrosion resistance in Simulated Body Fluid (SBF) solution. To date, no study has explored the use of g-C_3N_5 in combination with TiO_2 for developing corrosion-resistant coatings on 316LSS implants. Furthermore, there are no prior reports on utilizing this nanocomposite for orthopedic applications, despite the potential advantages of incorporating g-C_3N_5 into TiO_2 to enhance its properties. This study aims to develop and characterize TiO_2/g-C_3N_5 nanocomposite coatings for 316LSS implants, evaluate their electrochemical behavior, and assess their corrosion resistance in Simulated Body Fluid (SBF). Additionally, the

biocompatibility of the coatings will be assessed to determine their suitability for orthopedic applications. By addressing these objectives, this research seeks to advance the development of innovative corrosion-resistant coatings and establish g-C_3N_5 as a valuable material for biomedical applications.

2. Experimental

2.1 Materials

N-butanol ($C_4H_{10}O$) from RANKEM 99.0%, Titanium tetra isopropoxide (Ti (OCH $(CH_3)_2)_4$) from Sigma Aldrich (99.99 % purity), 3-Amino 1, 2, 4 triazole ($C_2H_4N_4$)-TCI, Hydrochloric acid solution (HCl)-Qualigens, Acetone $(CH_3)_2CO$, Ethanol (C_2H_5OH)-analytical grade reagents. Double distilled water was used throughout the experiment.

2.2 Preparation of 316LSS alloy sample

The chemical composition of 316LSS is shown in Table 1 [39]. The samples were fabricated from 316LSS and cut into 10 mm × 20 mm × 2 mm pieces. 80 to 2000 SiC paper was used to polish the metal at speeds between 200 and 900 rpm. After that, diamond paste was applied to provide a uniform, smooth surface texture. The sample was then cleaned in an ultrasonic bath using acetone, ethanol and distilled water. Finally, the polished 316LSS samples were used for further studies.

Table 1. Composition of the Simulated Body Fluid (SBF) solution used in the study, including concentrations of individual components and their respective molarities.

Order	Reagent	Amount (g)
1.	NaCl	12.052
2.	$NaHCO_3$	0.535
3.	KCl	0.337
4.	$K_2HPO_4.3H_2O$	0.346
5.	$MgCl_2.6H_2O$	0.477
6.	1.0 M – HCl	58.5ml
7.	$CaCl_2$	0.438
8.	Na_2SO_4	0.108
9.	Tris (hydroxymethyl) aminomethane	9.177

2.3 Coating preparation

A mixture of titanium tetra isopropoxide and n-butanol was stirred under constant magnetic stirring for two hours to obtain a TiO_2 solution. To prepare g-C_3N_5 powder, 3-Amino 1, 2, 4 triazole was sintered at 500°C for two hours. A foam-like powder was obtained and ground with a mortar. The powder was mixed with a 1M hydrochloric acid solution and placed in an ultrasonic cleaner. It was then sonicated for an hour. The powder was then repeatedly washed with deionised water. It was kept overnight in a hot air oven at 80°C. Different weights (0.01g, 0.03g, 0.05, 0.07g and 0.09g) of g-C_3N_5 were added to the prepared TiO_2 sol and stirred for 10 min. The suspension was subjected to ultrasonication for one hour. TiO_2/g-C_3N_5 (TiCN) sol was coated onto 316LSS at 4000 rpm for 20 seconds using a SPIN NXG-P1AC spin coater. The samples were sintered in a muffle furnace at 400°C for one hour after the coating process. The sintered samples were then collected and used for further investigation. The sintered samples were named as TiCN (0.01), TiCN (0.03), TiCN (0.05), TiCN (0.07) and TiCN (0.09) for further analysis.

2.4 Characterisation of sample

X-ray powder diffraction (XRD) spectra were collected utilising a Bruker D8 (Bruker AXS) diffractometer outfitted with a placement-sensitive detector. A CuKα lamp served as the irradiation source, emitting radiation with a wavelength of λ = 1.54Å. The crystal structure of the pure TiO_2, g-C_3N_5 and TiCN composite samples were analyzed. Samples were measured in the presence of infrared radiation, and chemical properties were observed using FTIR spectra in the 400–4000 cm^{-1} range. WITec ALPHA300 Raman spectroscopy was used to obtain the Raman spectra. An air-cooled laser was the exciting source, emitting radiation at 532 nm. Atomic force microscopy (AFM) (MFP-3D Origin Asylum Research AFM) Oxford instrument was used to measure the surface topography of the TiCN Coated 316LSS, and the surface morphology of the film was observed by scanning electron microscopy (SEM) using CARL ZEISS instrument at an acceleration voltage of 10kV.

2.5 Electrochemical Evaluation

Electrochemical measurements were carried out using a standard three-electrode cell. In this configuration, a saturated calomel electrode (SCE) served as the reference electrode, a platinum electrode as the counter electrode, and the test material as the working electrode. Simulated body fluid (SBF) was used as the electrolyte. Polarization measurements were conducted from cathodic to anodic directions at a scan rate of 1 mV/s. Corrosion rate was calculated using the tafel extrapolation method. The impedance measurements were taken in a frequency range of 100 kHz to 0.1 Hz, with an amplitude of 10 mV. Electrochemical behavior and corrosion resistance tests were conducted with seven 316LSS samples per condition, each measured in triplicate for reliability and statistical significance. These experiments were performed using a (BIOLOGIC VSP 300) potentiostat

operated by a personal computer with (EC Lab version 8.5) software.

2.6 Invitro Studies

In vitro studies using SBF are widely conducted to evaluate the biocompatibility of materials for biomedical applications [40-42]. Coated samples were soaked in an SBF solution for 14 days to observe hydroxyapatite growth. SBF was prepared following the procedure described in the referenced article [43].

3. Result and Discussion

3.1 X-Ray Diffraction Analysis

X-ray diffraction (XRD) analysis was performed to characterise the crystalline phases of the synthesized sample. As shown in Figure. 2, both TiO_2 and g-C_3N_5 exhibited well-defined single-phase crystal structures. In the case of TiO_2, the XRD pattern showed characteristic peaks at 25.2°, 37.5°, 47.9°, 53.7°, 54.8°, and 62.5°, corresponding to the (101), (004), (200), (105), (211), and (204) planes, which are indicative of the anatase phase [44]. For as-synthesized g-C_3N_5, the XRD pattern displayed a prominent peak at 27.6°, corresponding to the (002) plane, associated with the tighter packing of carbon nitride layers, consistent with JCPDS card no. 87-1526 [45,46]. Additionally, a broadened (002) peak with decreased intensity was observed for acid-treated g-C_3N_5 nanosheets, indicating exfoliation of the bulk material into fewer-layer nanosheets. This suggests that the bulk g-C_3N_5 was successfully exfoliated into smaller sheets. The TiCN composite displayed similar diffraction peaks as pure TiO_2, suggesting that the crystal phase of TiO_2 remained unchanged in the presence of g-C_3N_5. However, slight variations in peak positions were observed in the composite, and some peaks showed increased intensity, indicating intricate packing interactions between g-C_3N_5 and TiO_2. Due to the relatively low amount of g-C_3N_5 in the TiCN composite, the prominent diffraction peaks for g-C_3N_5 were not observed [47]. No additional phases were detected beyond TiO_2 and g-C_3N_5, confirming the purity of the TiCN compositions.

3.2 FT-IR Analysis

FTIR analysis was used to investigate the elements in TiO_2, g-C_3N_5, and TiCN samples are shown in Figure 3. The TiO_2 sample shows a broad band between 500 and 900 cm^{-1}, which may result from the formation of Ti-O and Ti-O-Ti bonds as the titanium dioxide. This broadening might also be due to the titanium dioxide film caused by carbon or hydroxyl groups in the Ti-O system [48, 49]. The g-C_3N_5 sample results in a peak at around 3100 cm^{-1} originates from the stretching vibration of -NH_2 and -OH groups from water molecules adsorbed on the surface. The band between 1650 and 1250 cm^{-1} is due to the typical stretching of heterocyclic C=N units, while the peak at about 802 cm^{-1} represents the breathing vibration of triazine units. The peak near 1500 cm^{-1}, slightly shifted to a lower wavenumber and broadened compared to g-C_3N_5, suggests the formation of protonated g-C_3N_5, likely due to hydrolysis of C_3N_5 after acidification. This change also leads to the appearance of a C-O stretching peak at 1080 cm^{-1}. The broadened absorption peaks between 3500 and 3000 cm^{-1} for -NH- or -NH_2 groups indicate that hydrogen bonds involving -NH-/-NH_2 were distorted [50, 51]. In the TiCN composites, the bands between 500 and 900 cm^{-1} are characteristic of TiO_2, and the peaks between 3600 and 3800 cm^{-1} correspond to g-C_3N_5, confirming the interaction between TiO_2 and g-C_3N_5 in the TiCN composite.

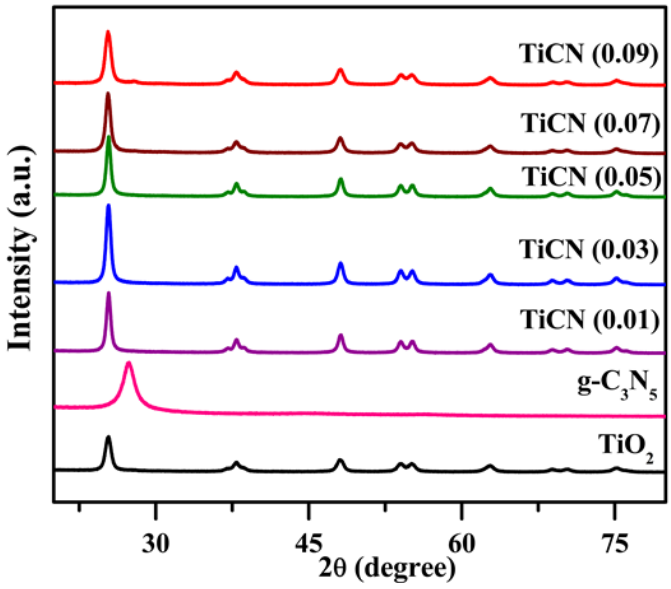

Figure 2. XRD patterns showing the structural and crystalline characteristics of the sample and their composites

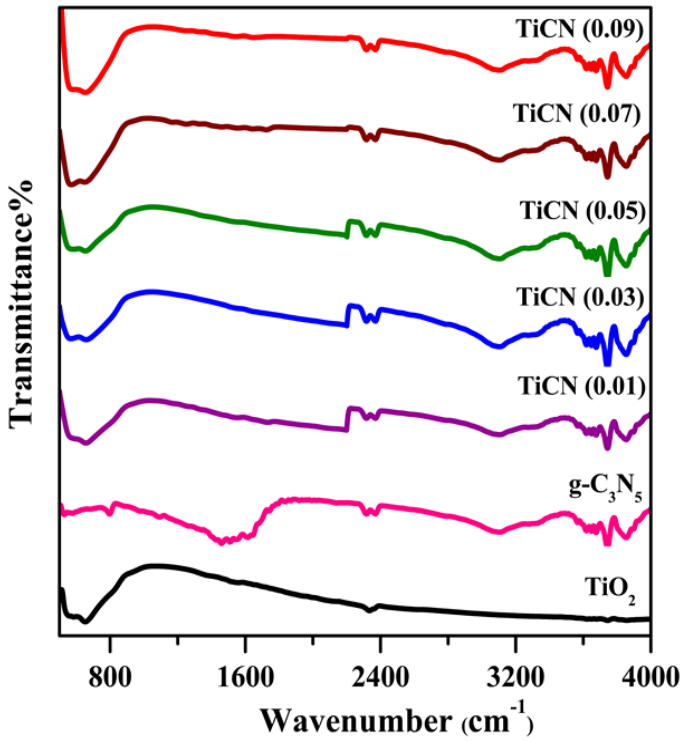

Figure 3. FTIR spectra showing characteristic absorption peaks of TiO_2, g-C_3N_5, and TiCN composites

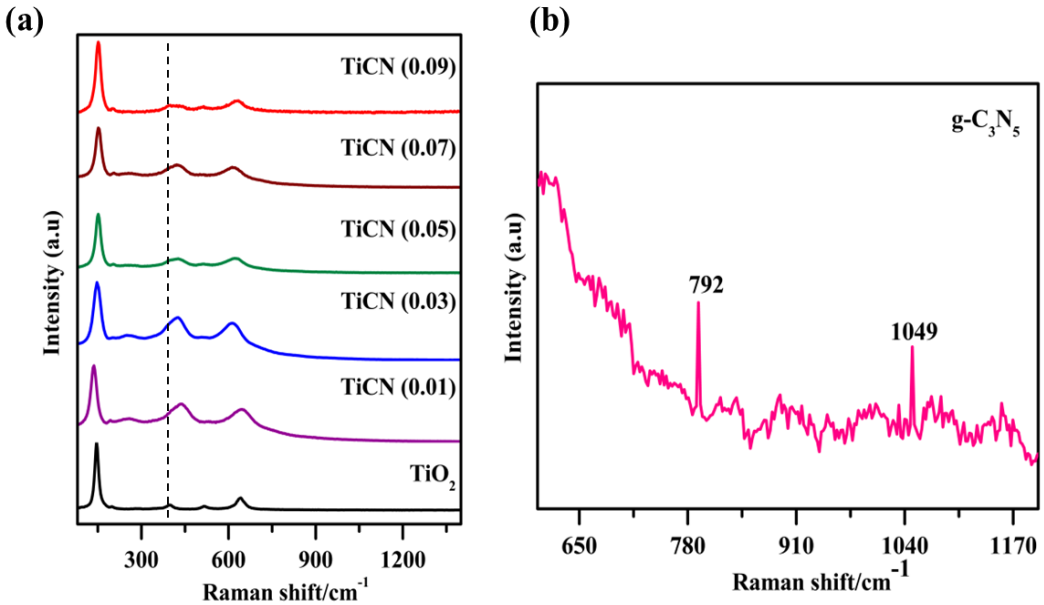

Figure 4. Raman spectra of TiO_2, g-C_3N_5, and TiCN composites, highlighting the characteristic vibrational modes and structural features of each sample and their composites

3.3 Raman Analysis

Raman spectroscopy was used to examine the crystalline structure and detect any trace amounts of secondary phases or impurities in the samples, as shown in the Figure 4 [52]. In Figure 4a, the bands observed at 145 cm^{-1} (Eg), 197 cm^{-1} (Eg), 396 cm^{-1} (B1g), 516 cm^{-1} (B1g), and 640 cm^{-1} (Eg) confirm the characteristic properties of TiO_2 anatase [53]. The strong correlation between the Raman and XRD data verifies the high-purity TiO_2 anatase phase prepared through sol-gel synthesis [54, 55]. Figure. 4b shows bands at 792 cm^{-1} and 1049 cm^{-1}, indicating the presence of the g-C_3N_5 phase. The Raman spectra for TiCN composites show peaks that are slightly shifted from those of pure TiO_2. Due to the lower concentration of g-C_3N_5, the TiCN composite peaks closely resemble the characteristic peaks of pure TiO_2. These shifts result in peak broadening in the Raman spectra, confirming the presence of both TiO_2 and g-C_3N_5 in the composite and indicating that the peak shifts arise from changes in

material composition rather than chemical composition. Variations in g-C_3N_5 content influence the structural properties of the composite, as confirmed by Raman spectroscopy, and this data aligns well with XRD. This peak broadening and the observed blue shifts from the positions of TiO_2 suggest increased bonding interactions resulting from structural integration between TiO_2 and g-C_3N_5.

3.4 Scanning Electron Microscopy Analysis

Figure 5 reveals SEM micrographs of uncoated 316LSS and coated with TiO_2, g-C_3N_5 and TiCN coating. In Figure 5A, the SEM image of the uncoated sample reveals prominent grid lines resulting from mechanical polishing of 316LSS [56-58].

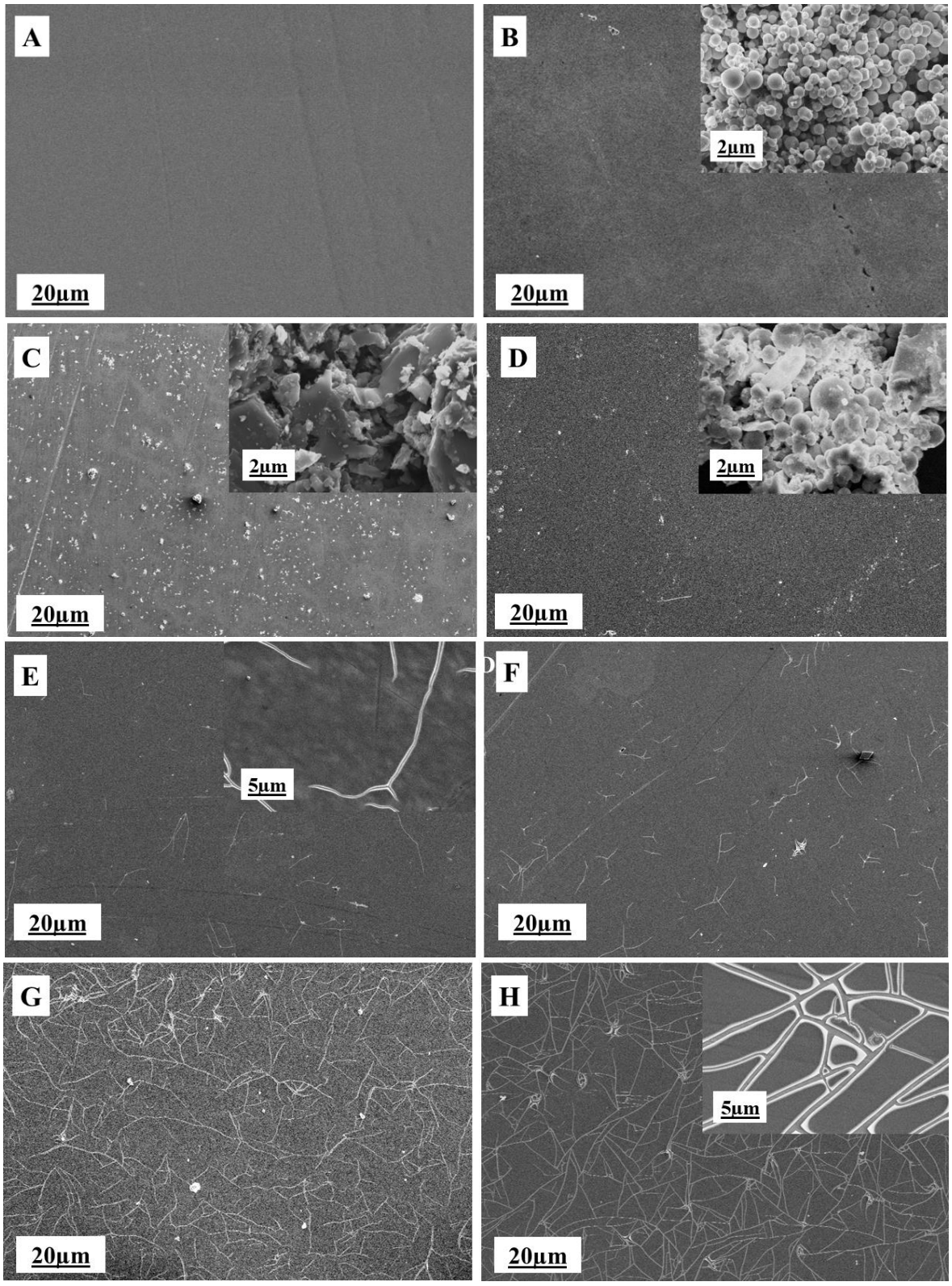

Figure 5. SEM images of A) Bare B) TiO_2 C) g-C3N5D) TiCN (0.01) E) TiCN (0.03) F) TiCN (0.05) G) TiCN (0.07) H) TiCN (0.09), while a magnified view highlights structural detail

Figure 5B shows a TiO_2-coated surface with dense and porous surface morphology, and at magnification, a uniform sphere shape structure was observed [59]. Figure 5C shows the SEM micrograph of the g-C_3N_5-coated sample, showing flat nanosheets with occasional larger agglomerates, and at magnification, stacked sheets-like structures are observed. Figure 5D illustrates the TiCN (0.01) coated sample, which shows a reduced pore size and homogeneous surface and suggests improved coating properties due to the interaction of TiO_2 and g-C_3N_5. These improved surface properties reveal the g-C_3N_5 matrix embedded in the TiO_2. TiCN (0.03) coated sample has enhanced surface properties compared to 0.01 TiCN coating, as shown in Figure. 5E. Beyond the TiCN 0.03 weight percentage, the coating starts to crack due to the thickness of the coating as well as the fast solvent evaporation during the sintering process, which gradually develops the cracks [60-62]. Compared to 0.05, 0.07 and 0.09, weight percentages of TiCN coating have larger cracks, as shown in Figure. 5F, 5G, 5H, which highlights the importance of controlling coating thickness for maintaining mechanical integrity [63]. This uniformity in the coating is crucial to the stability and longevity of orthopedic implants, as it produces a strong mechanical bond between the implant and the surrounding bone tissue [64].

3.5 Atomic force microscopy analysis

Figure 6A shows AFM images of an uncoated 316LSS sample, which has grid lines resulting from mechanical polishing are well corroborated with obtained SEM results. The mean square roughness (Rrms) value of 1.8 nm and an average roughness (Ra) value was 1.3 nm was calculated. Figure 6B shows the TiO_2-coated sample, featuring a uniform spherical structure that creates a highly porous surface. The TiO_2 coating has a root mean square roughness (Rrms) of 8.8 nm, average roughness (Ra) of 7.1 nm, and average particle size of approximately 50 nm was observed. The g-C_3N_5 coating in Figure. 6C results in flat nanosheets with occasional larger agglomerates adhering on the surface of the sample, which has an average particle size of around 70 – 100 nm. It has a lower surface roughness value Rrms 5.5 nm, Ra 3.2 nm compared to TiO_2 because flat portions are smooth stacked layers, contributing to low roughness. In contrast, agglomerated particles contribute to heightening of the peaks. In addition, Fig. 6D, 6E, 6F, 6G, and 6H display the TiCN composite coating with different weight proportions. It was well-connected sphere shape structures and increased thickness from 0.01 to 0.09 compared to both TiO_2 and g-C_3N_5 coatings, indicating successful incorporation of the g-C_3N_5 into TiO_2 sample and the surface roughness values is TiCN (0.01) Rrms 6.1 nm, Ra 4.8 nm, TiCN(0.03) Rrms 6.7 nm, Ra 5.3 nm, TiCN(0.05) Rrms 7 nm, Ra 5.6 nm, TiCN(0.07) Rrms 7.1 nm, Ra 6.0 nm, TiCN(0.09) Rrms 7.3 nm, Ra 5.6 nm. Higher roughness values suggest a larger pore diameter, which facilitates the incorporation of hydroxyapatite into the pores and improves the bioactivity of the coated surface [65-68]. The surface topography results align well with obtained SEM results.

Figure 7 illustrates the line profile, the significant depth, and the height, indicating that the nanometer to sub-micrometer of the pore's presence was observed. The average particle size of the TiCN composite was around 25-100 nm. This suggests that bioactivity is closely related to the curvature of the particles on the coated film surface [69]. The porous nature of the coating sample promotes bone in-growth, leading to a strong attachment to the bone [70].

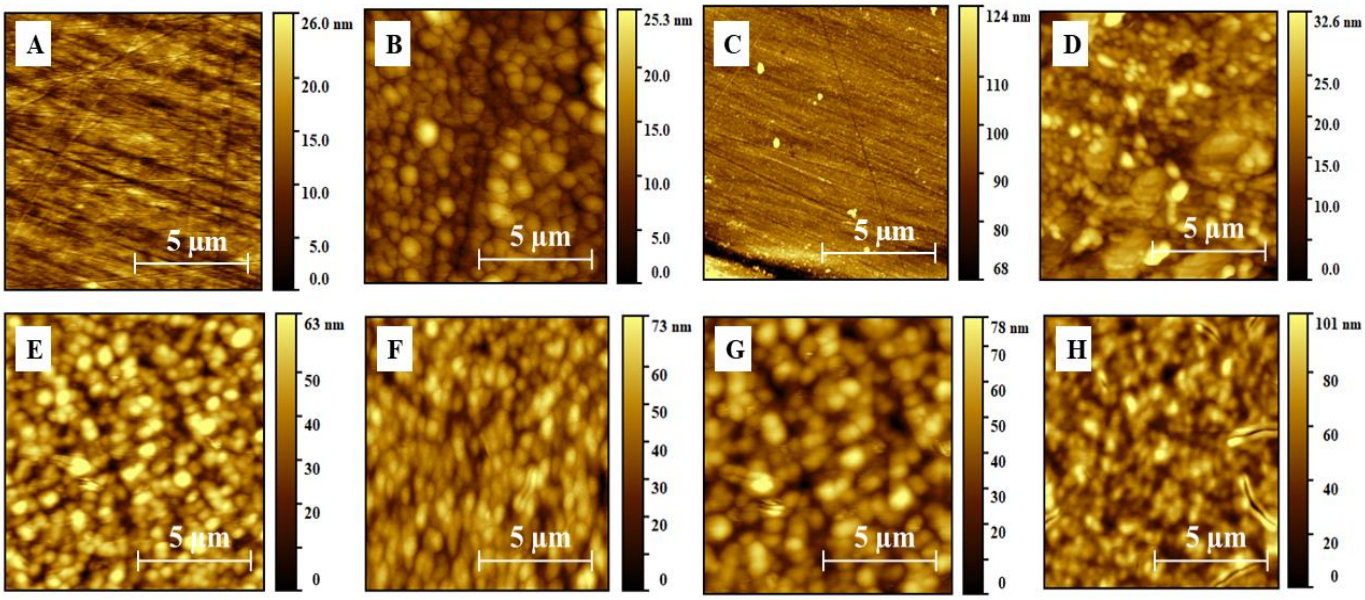

Figure 6. AFM 2D images of A) Bare B) TiO2 C) g-C3N5 D) TiCN (0.01) E) TiCN (0.03) F) TiCN (0.05) G) TiCN (0.07) H) TiCN (0.09) composites

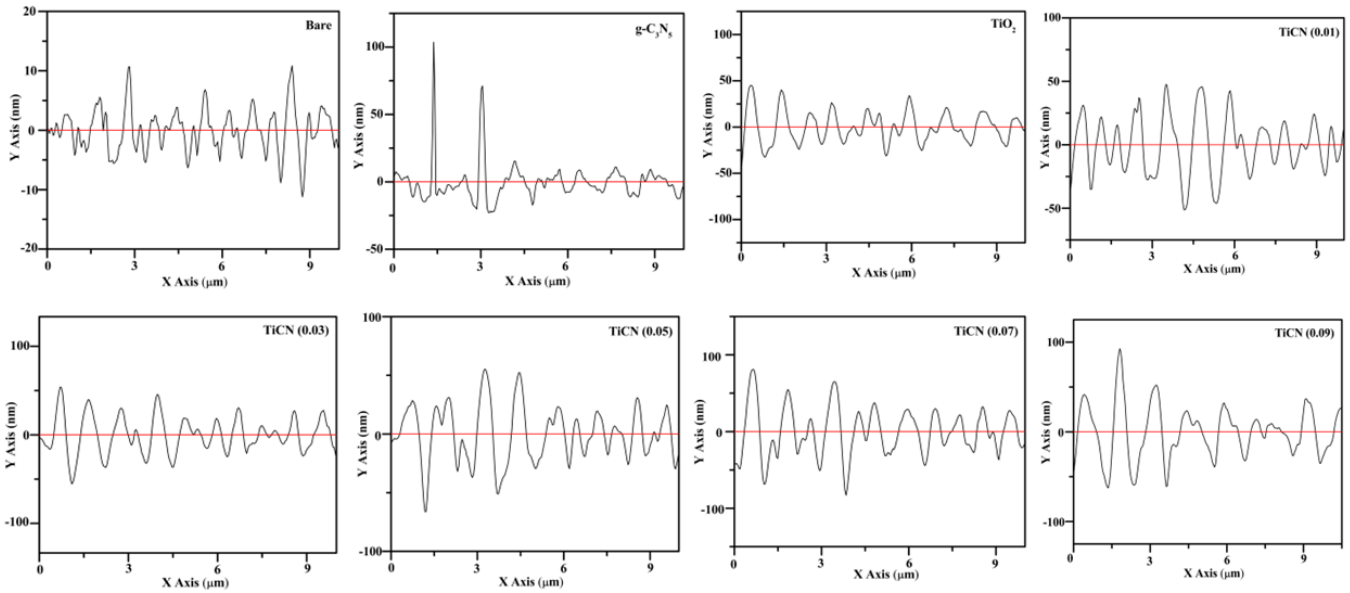

Figure 7. AFM line profile of the uncoated and coated sample, showing the surface roughness and topographical variations across different regions of the sample

These findings suggest that the synergistic interaction between TiO_2 and g-C_3N_5 in TiCN composite can potentially improve the biocompatibility of coatings.

3.6 Open Circuit Potential

In Figure. 8, OCP measurements showed that the coated samples exhibited higher corrosion resistance than the uncoated 316LSS. The TiO_2, g-C_3N_5 and TiCN composite coatings demonstrated a positive shift in OCP values, indicating the formation of protective films. The TiCN (0.03 wt%) composite has the highest OCP value of -0.37 V vs SCE, reflecting superior corrosion resistance. Higher g-C_3N_5 concentrations (0.05, 0.07, and 0.09 wt%) showed decreased corrosion resistance due to crack formation in the coated film. Therefore, the TiCN (0.03 wt%) composite coating exhibits the enhanced corrosion protection, while the TiO_2 and g-C_3N_5 coatings showed moderate corrosion protection properties. The positive OCP shift indicates effective corrosion protection [71-73]. The superior corrosion resistance of the TiCN (0.03 wt%) composite coating can be attributed to the optimal concentration of TiCN that promotes the formation of a stable, protective film and avoids structural defects that could compromise the coating's performance. The enhanced OCP shift confirms the positive contribution of TiCN to corrosion protection, while the results from TiO_2 and g-C_3N_5 coatings demonstrate moderate protection in comparison. These results confirm that adding nitrogen-rich carbon nitrite enhances the OCP of the TiCN composite coating.

3.7 Potentiodynamic polarization studies

To investigate the corrosion protection properties of the TiCN sample, a polarization test was conducted, and the corresponding results are presented in Figure 9. The Tafel method was used to extrapolate corrosion potential, corrosion current density and corrosion rate from polarization curves, which are all typically recognized as important parameters for determining corrosion resistance [74, 75]. Generally, the lowest current density and more positive potential indicate better corrosion resistance [76]. For the uncoated 316LSS, the values were determined to be -0.73 V vs SCE -1.9 µA and 0.045 mmpy, respectively. In the case of TiO_2, the potential -0.57 V vs SCE, current density -2.4 µA and corrosion rate 0.012 mmpy values were obtained, which has enhanced corrosion resistance than bare. For g-C_3N_5, the absence of a straight-line section confirms the presence of coating. It has a corrosion potential of -0.68 V vs SCE, a current density of -1.7 µA and a corrosion rate of 0.037 mmpy. However, its corrosion rate is almost the same as that of the uncoated 316LSS due to the low adhesive nature of the coating. TiCN (0.03%) composite coated sample exhibited a high positive corrosion potential of -0.35 V vs SCE and low current density of -2.1 µA with a corrosion rate of 0.003 mmpy compared to another TiCN coated sample. The lowest Icorr observed for the TiCN coating can be attributed to the strong interfacial interaction between the TiCN coating and the sample, likely due to the high adhesive strength of this coating [77]. The polarization curves bend towards lower current values in the anodic region, indicating that the metal sample has entered a passive state.

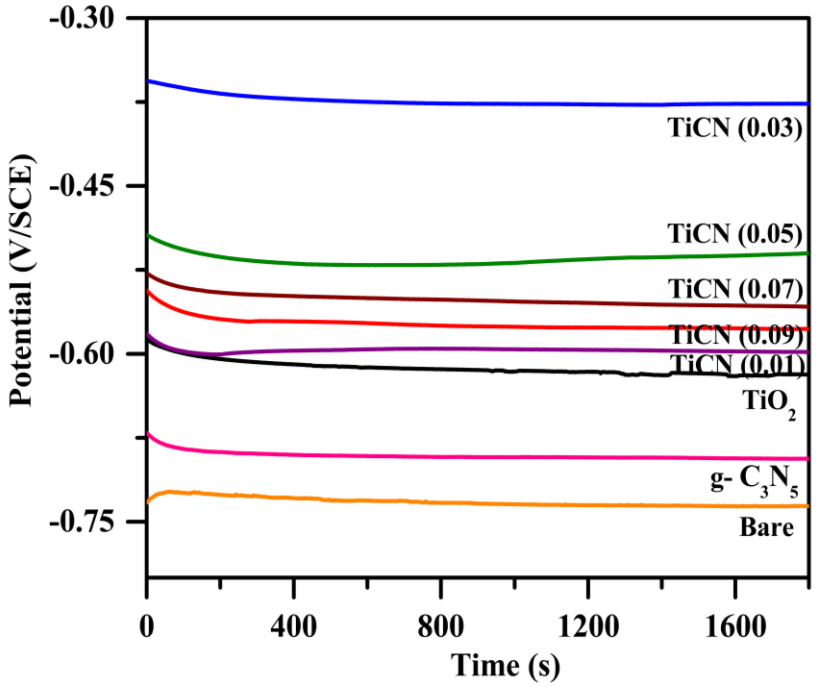

Figure 8. Open circuit potential profiles of uncoated and coated samples

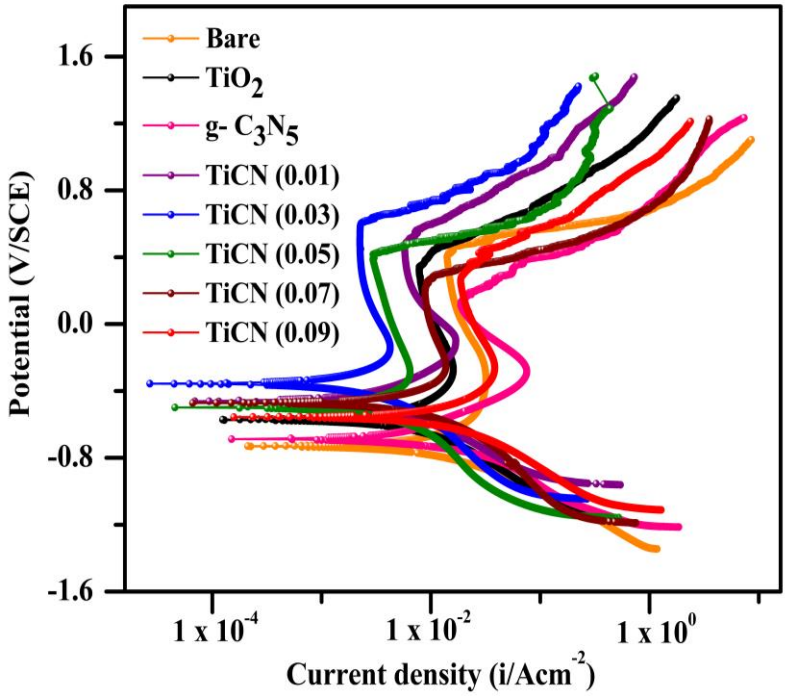

Figure 9. potentiodynamic polarisation graph for uncoated and coated materials

This forms a protective layer like passive film on the metal surface, which significantly slows down the corrosion process [78, 79]. This improvement was due to the TiCN coating on the sample, which hinders the electrolyte solution from reaching the metal sample, leading to a lower current density and increase in corrosion protection efficiency. Potentiodynamic polarization studies confirmed that the TiCN (0.03%) coating has four times higher corrosion potential, significantly improving the corrosion protection performance of the 316LSS sample in the SBF solution.

3.8 Electrochemical impedance spectroscopy

Figure 10A shows the impedance spectra for both coated and uncoated samples, where the uncoated sample exhibits a single semicircle. In contrast, the coated samples showed two semicircles, magnified in Figure. 10B. The initial small semicircle corresponds to the coating layer, with the radius increasing due to the coating. In Figure. 10, the uncoated 316L stainless steel has lower resistance due to the electrolyte penetration occurring through conductive paths in surface pores [80-

82]. However, for the g-C_3N_5-incorporated TiO_2 coating, these conductive paths are less accessible due to smaller pore size and higher compactness, which slows electrolyte reach to the sample compared to TiO_2 and g-C_3N_5. Solution resistance (Rs) depends on the area available for current and the resistivity of the electrolyte, showing minimal variation across samples. An increase in charge transfer resistance (Rct) at the metal/electrolyte interface reduces corrosion rate by slowing electron movement and limiting material deterioration [83]. The TiCN (0.03%) coating shows a high solution resistance (23 Ωcm²) and charge transfer resistance (197 Ωcm²), suggesting strong corrosion resistance in the electrolyte solution. The equivalent circuits depicted in Figure 11, used for EIS data analysis, incorporate Rs, representing the electrolyte resistance between the working and reference electrodes. Rct and R_1 correspond to the charge transfer resistances for the uncoated and coated samples. The elements Q_{dl} and Q_1 represent the capacitive components associated with the uncoated and coated samples [84, 85]. Surface, which is typically lower for materials that are more prone to corrosion. The increased Rct value in this case is a clear indication that the TiCN (0.03%) coating effectively prevents corrosive ions from interacting with the underlying substrate, making it an excellent barrier. The higher Q1 values for the TiCN (0.03%) composite suggest that a more stable and compact oxide layer forms compared to the uncoated and other TiCN-coated samples, which contributes to enhanced corrosion protection. Additionally, the TiCN (0.03%) composite coating outperforms other TiCN concentrations in corrosion resistance. This is likely because of the TiCN particles are well-dispersed, facilitating the formation of a dense and continuous protective layer. Therefore, the TiCN (0.03%) composite demonstrates superior corrosion resistance than other TiCN coating.

3.9 In-vitro Characterization

3.9.1 Scanning Electron Microscopy Analysis

Figure 12 shows SEM micrographs of uncoated 316LSS and sample coated with TiO_2, g-C_3N_5, and TiCN composites after 14 days of immersion in SBF solution, highlighting differences in hydroxyapatite (HAP) formation across these surfaces. Figure 12A illustrates the SEM micrograph of the uncoated 316LSS sample. Randomly agglomerated spherical particles are observed, signifying the formation of hydroxyapatite (HAP). This growth was attributed to the inherent bioactivity of surgical-grade 316LSS, which promotes HAP deposition due to its favorable interaction with biological fluids [86]. Figure 12B shows the TiO_2 coated sample. TiO_2 encourages HAP nucleation and growth on its surface, contributing to improved bone-cell interaction. Figure 12C displays the g-C_3N_5 coated sample, where the formation of HAP appears more prominent compared to both the uncoated and the TiO_2 coated sample. This enhanced HAP layer was attributed to the biocompatibility of the g-C_3N_5 coating, which supports increased HAP nucleation and crystallization [87]. Figure 12D reveals the TiCN composite coating, which exhibits a dense, closely packed spherical shape structure with an interconnected surface, indicating better adhesion with higher bioactivity-induced layers than the other samples. The SBF solution penetrates into the pores of the TiCN coated samples, promoting the formation of a hydroxyapatite-rich layer [88]. It has been reported that bioactive implant materials possessing a bilayer passive film with an inner barrier and outer porous layer encourage better osseointegration and bone tissue integration [89].

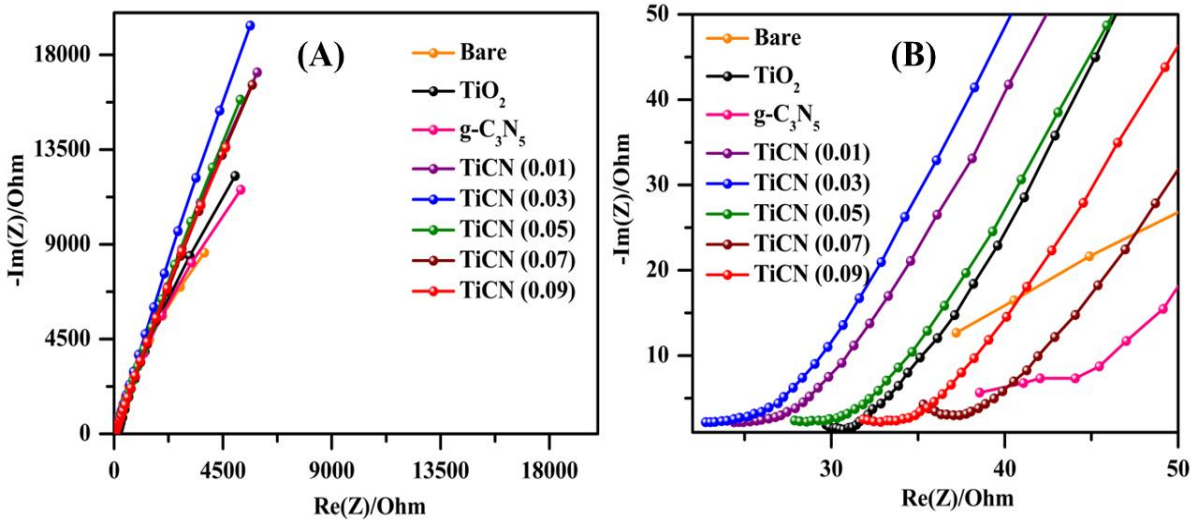

Figure 10. Impedance spectroscopy of A) uncoated and coated sample B) Magnified view of uncoated and coated sample

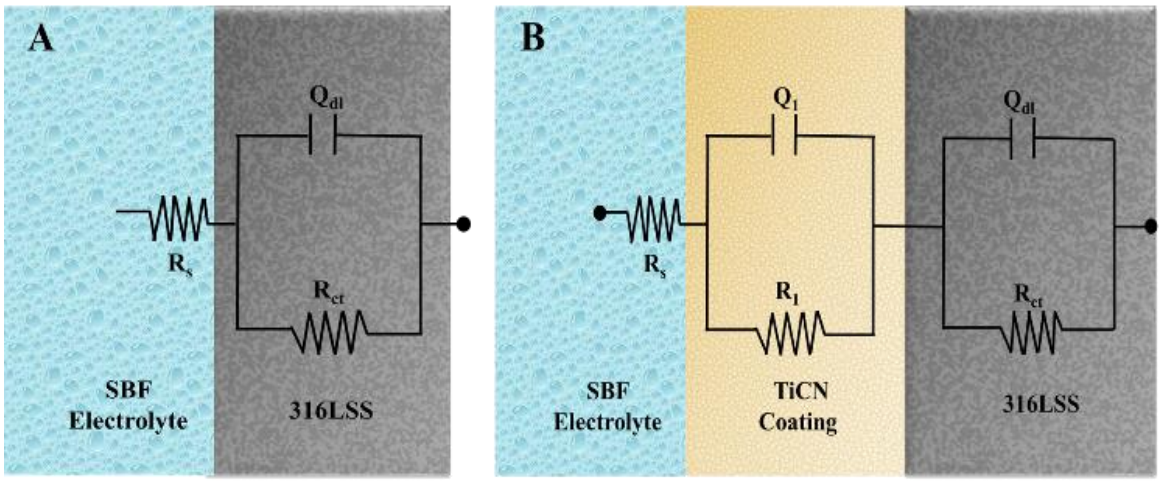

Figure 11. Equivalent circuit diagrams for A) Uncoated 316LSS B) TiCN Coated 316LSS

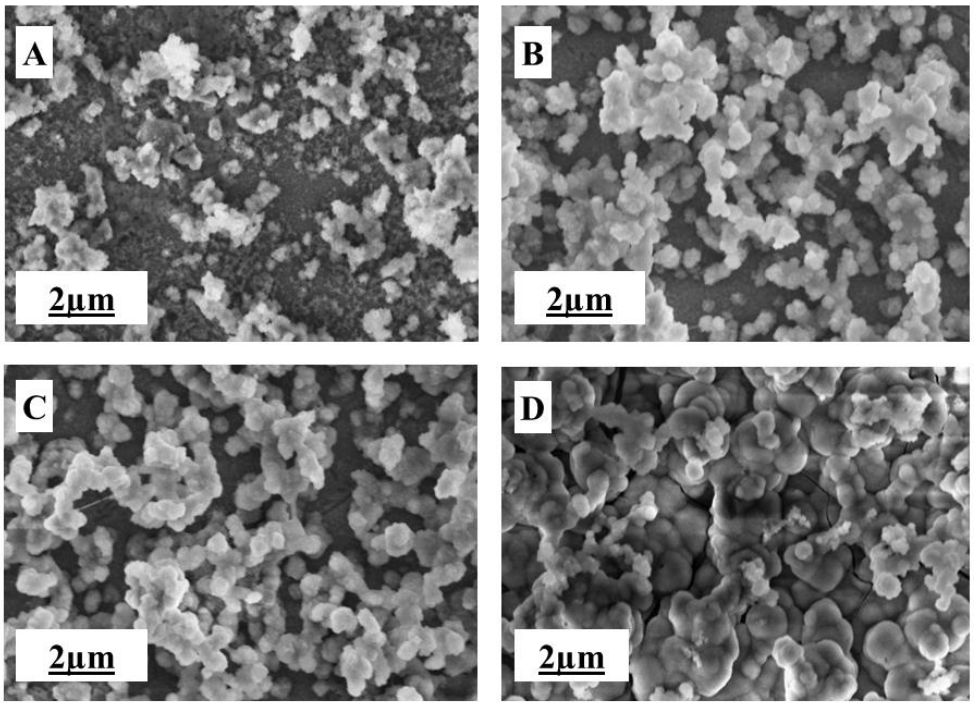

Figure 12. In vitro analysis of the sample: A) Bare B) TiO_2 C) g-C_3N_5 and D) TiCN (0.03%) composite coating after immersion in simulated body fluid solution

3.10 Raman analysis

Raman spectroscopy is a powerful tool for mineral analysis [90]. The successful deposition of HAP growth was confirmed by the Raman spectrum presented in Figure 13. The characteristic peak of the phosphate ion, associated with the fully symmetric P−O−P stretching mode in HAP, was observed between 954 cm^{-1} and 962 cm^{-1}. The band between 120 cm^{-1} to 300 cm^{-1} corresponds to Ca-PO_4 in a double-bending mode, while the bands from 582 cm^{-1} to 595 cm^{-1} and 611 cm^{-1} to 649 cm^{-1} are attributed to PO_4^{3-} in a triply degenerate bending mode. The peak between 1034 cm^{-1} to 1087 cm^{-1} corresponds to the triply degenerate antisymmetric stretching mode of PO_4^{3-}. The observed Raman bands align well with literature findings [91, 92]. Furthermore, the increased intensity of the TiCN peak clearly indicates that hydroxyapatite formation significantly enhanced the composites compared to g-C_3N_5 and TiO_2 coatings. The Raman spectrum clearly shows that g-C_3N_5 and TiO_2 coatings exhibit fewer peaks related to hydroxyapatite formation than the TiCN composite. The growth of phosphate ions (PO_4^{3-}) on metal surfaces during hydroxyapatite deposition enhances the bioactivity of the implants [93]. The calcium and phosphate ions present in the hydroxyapatite (HAp) improve the biological activity of implants by releasing ions during implantation, which supports bone regeneration [94]. Therefore, the TiCN coating was considered biocompatible due to its tissue bonding characteristics. This indicates that the TiCN coating was more effective for biomedical applications.

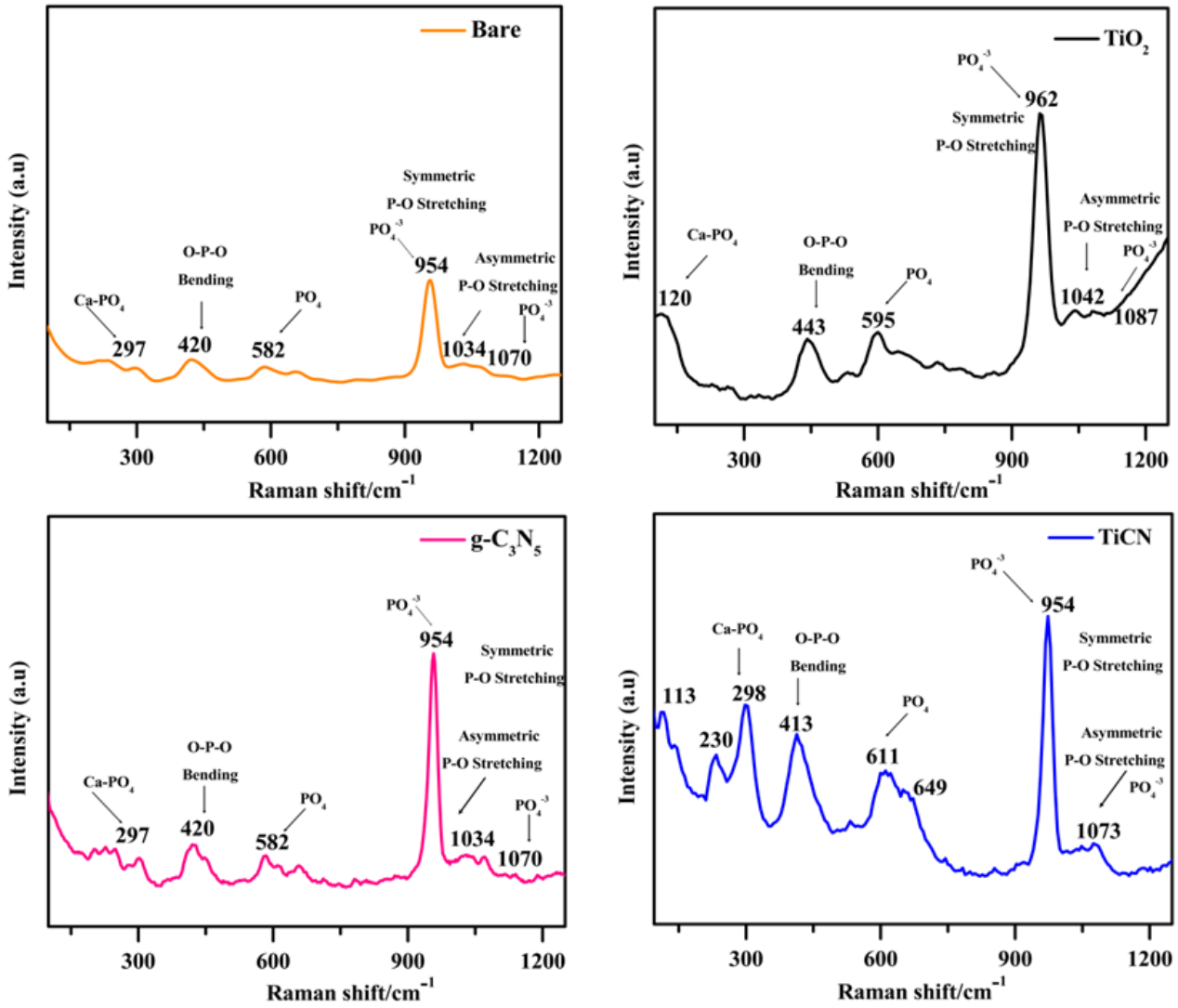

Figure 13. Raman spectrum of HAP deposition on bare, TiO_2, g-C_3N_5, and TiCN (0.03%) composite after the immersion in SBF solution

4. Conclusion

The corrosion performance of the 316LSS sample was assessed after coating with varying weight percentages of TiCN composites. XRD, FT-IR, Raman, AFM, and SEM analyzes confirmed TiO_2 and g-C_3N_5 presence, verifying successful TiCN deposition. Electrochemical analyzes identified the TiCN 0.03% composite as optimal, showing significantly improved corrosion resistance with reduced current density and increased polarisation resistance in SBF solution compared to uncoated and other coated samples. In vitro studies further demonstrated that the TiCN (0.03%) composite supports hydroxyapatite (HAP) growth after 14 days in SBF, with SEM revealing a dense HAP layer for TiCN (0.03%). These findings suggest that the TiCN (0.03%) composite coating was a highly promising protective layer for 316LSS implants, offering superior corrosion resistance and biocompatibility in physiological environments. The TiCN (0.03%) composite coating can be scaled for industrial applications through optimized coating techniques and efficient production processes.

References

[1] M. Niinomi, (Recent metallic materials for biomedical applications. Metallurgical and materials transactions A, 33, (2002) 477-486. https://doi.org/10.1007/s11661-002-0109-2

[2] Y. Zhu, W. Liu, T. Ngai, Polymer coatings on magnesium-based implants for orthopedic applications. Journal of Polymer Science, 60(1), (2022) 32-51. https://doi.org/10.1002/pol.20210578

[3] M.H. Nawaz, A. Aizaz, A.Q. Ropari, H. Shafique, O.B. Imran, B.Z. Minhas, J. Manzur, M.S. Alqahtani, M. Abbas, M.A. Ur Rehman, A study on the effect of bioactive glass and hydroxyapatite-loaded Xanthan dialdehyde-based composite coatings for potential orthopedic applications. Scientific Reports, 13(1), (2023) 17842. https://doi.org/10.1038/s41598-023-44870-5

[4] M. Benčina, A. Iglič, M. Mozetič, I. Junkar, Crystallized TiO2 nanosurfaces in biomedical applications. Nanomaterials, 10(6), (2020) 1121.

https://doi.org/10.3390/nano10061121

[5] C.H.M. Beraldo, A. Spinelli, N. Scharnagl, T.F. da Conceição, Phosphorylated PVA coatings for corrosion protection of Mg AZ31 alloy. Journal of Coatings Technology and Research, 21(1), (2024) 243-253. https://doi.org/10.1007/s11998-023-00813-3

[6] M. Poorraeisi, A. Afshar, The study of electrodeposition of hydroxyapatite-ZrO2-TiO2 nanocomposite coatings on 316 stainless steel. Surface and Coatings Technology, 339, (2018) 199-207. https://doi.org/10.1016/j.surfcoat.2018.02.030

[7] M. Ramezani, Z.M. Ripin, An overview of enhancing the performance of medical implants with nanocomposites. Journal of Composites Science, 7(5), (2023) 199. https://doi.org/10.3390/jcs7050199

[8] C.C. Wachesk, S.H. Seabra, T.A.T. Dos Santos, V.J. Trava-Airoldi, A.O. Lobo, F.R. Marciano, In vivo biocompatibility of diamond-like carbon films containing TiO2 nanoparticles for biomedical applications. Journal of Materials Science: Materials in Medicine, 32(9), (2021)117. https://doi.org/10.1007/s10856-021-06596-6

[9] S. Jafari, B. Mahyad, H. Hashemzadeh, S. Janfaza, T. Gholikhani, L. Tayebi, Biomedical applications of TiO2 nanostructures: recent advances. International journal of nanomedicine, (2020) 3447-3470. https://doi.org/10.2147/IJN.S249441

[10] A.M. Bannunah, Biomedical applications of zirconia-based nanomaterials: challenges and future perspectives. Molecules, 28(14), (2023) 5428. https://doi.org/10.3390/molecules28145428

[11] E. Fiorentis, M.A. Gatou, N.E. Lagopati, A. Pavlatou, Biomedical Applications of Silica (SiO2) Nanoparticles. Biomedical Journal of Scientific & Technical Research, 51(10, (2023) 42382-42389. http://dx.doi.org/10.26717/BJSTR.2023.51.008057

[12] P.A. Hassanpour, Y. Panahi, A. Ebrahimi-Kalan, A. Akbarzadeh, S. Davaran, A.N. Nasibova, R. Khalilov, T. Kavetskyy, Biomedical Applications of Aluminium Oxide Nanoparticles. micro & Nano Letters, 13(9), (2018)1227-1231. https://doi.org/10.1049/mnl.2018.5070

[13] A. Fujishima, X. Zhang, D.A. Tryk, TiO_2 photocatalysis and related surface phenomena. Surface science reports, 63(12), (2008) 515-582. https://doi.org/10.1016/j.surfrep.2008.10.001

[14] M. Priyadarshini, U. Rama Chetan, U. Vijayalakshmi, Bioactive Coating as a Surface Modification Technique for Biocompatible Metallic Implants: A Review. Journal of Asian Ceramic Societies, 7(4), (2019) 397-406. https://doi.org/10.1080/21870764.2019.1669861

[15] A.M. Kumar, N. Rajendran, Electrochemical aspects and in vitro biocompatibility of polypyrrole/TiO2 ceramic nanocomposite coatings on 316L SS for orthopedic implants. Ceramics International, 39(5), (2013) 5639-5650. https://doi.org/10.1016/j.ceramint.2012.12.080

[16] K.T. Oh, Y.S. Park, Plasma-sprayed coating of hydroxylapatite on super austenitic stainless steels. Surface and Coatings Technology, 110(1-2), (1998) 4-12. https://doi.org/10.1016/S0257-8972(98)00537-4

[17] J. Dai, J. Yang, L. Zhuge, X. Wu, Al2O3–TiO2 composite coatings with enhanced anticorrosion properties for 316L stainless steel. Materials and Corrosion, 71(9), (2020) 1512-1520. https://doi.org/10.1002/maco.201911449

[18] B. Garrido, V. Albaladejo-Fuentes, I.G. Cano, S. Dosta, Development of bioglass/PEEK composite coating by cold gas spray for orthopedic implants. Journal of Thermal Spray Technology, (2022)1-11. https://doi.org/10.1007/s11666-021-01312-w

[19] O. Levana, J.H. Jeong, S.S. Hur, W. Seo, M. Lee, K.M. Noh, S. Hong, J.H. Park, J.H. Lee, C. Choi, Y. Hwang, Development of nanoclay-based nanocomposite surfaces with antibacterial properties for potential biomedical applications. Journal of Industrial and Engineering Chemistry, 120, (2023) 448-459. https://doi.org/10.1016/j.jiec.2022.12.052

[20] Z. Aouzal, M. Bouabdallaoui, A. El Guerraf, S. Ben Jadi, M. Bazzaoui, R. Wang, E.A. Bazzaoui, Electrochemical, spectroscopic and microscopic investigation of PEDOT coated nickel plate from aqueous micellar solutions and its anti-corrosion performances. Journal of Coatings Technology and Research, 20(3), (2023) 1053-1068. https://doi.org/10.1007/s11998-022-00724-9

[21] G. Liao, F. He, Q. Li, L. Zhong, R. Zhao, H. Chee, H. Gao, B. Fang, Emerging graphitic carbon nitride-based materials for biomedical applications. Progress in Materials Science, 112, (2020) 100666. https://doi.org/10.1016/j.pmatsci.2020.100666

[22] D. Rane, S. Kerkar, S.R. Ramanan, M. Kowshik, Superwettable surfaces and factors impacting microbial adherence in microbiologically-influenced corrosion: a review. World Journal of Microbiology and Biotechnology, 40(3), (2024) 98. https://doi.org/10.1007/s11274-024-03886-3

[23] G. Yang, T. Chen, B. Feng, J. Weng, K. Duan, J. Wang, X. Lu, Improved corrosion resistance and biocompatibility of biodegradable magnesium alloy by coating graphite carbon nitride (g-C3N4). Journal of Alloys and Compounds, 770, (2019) 823-830. https://doi.org/10.1016/j.jallcom.2018.08.180

[24] Q. Fu, M. Feng, J. Li, N. He, W. Li, J. Li, J. Yang, W. Jin, W. Li, Z. Yu, Effects of hydroxyapatite coatings on enhanced corrosion protection and cytocompatibility of high-purity magnesium. Journal of Coatings Technology and Research, 19(6), (2022)1757-1771. https://doi.org/10.1007/s11998-022-00646-6

[25] A. Khaskhoussi, L. Calabrese, M. Curro, R. Ientile, J. Bouaziz, E. Proverbio, Effect of the Compositions on the Biocompatibility of New Alumina–Zirconia–Titania Dental Ceramic Composites. Materials. 13 (2020) 1374. https://doi.org/10.3390/ma13061374

[26] N. Hallemans, D. Howey, A. Battistel, N.F. Saniee, F. Scarpioni, B. Wouters, F. La Mantia, A. Hubin, W.D. Widanage, J. Lataire, Electrochemical Impedance Spectroscopy Beyond Linearity and Stationarity—A Critical Review. Electrochimica Acta, 466, (2023) 142939. https://doi.org/10.1016/j.electacta.2023.142939

[27] P. Raymond, F. St-Germain, S. Paul, D. Chabot, L. Deschênes, Impact of Nanoparticle-Based TiO_2 Surfaces on Norovirus Capsids and Genome Integrity. Foods. 13, (2024) 1527. https://doi.org/10.3390/foods13101527

[28] M.S. Nagare, A. Hakami, P.K. Biswas, E.K. Stefanakos, S.S. Srinivasan, A Review of Thermochromic Materials for Coating Applications: Production, Protection, and Degradation of Organic Thermochromic Materials. Journal of Coatings Technology and Research, 22, (2025) 91–115. https://doi.org/10.1007/s11998-024-00982-9

[29] C. García-Cabezón, V. Godinho, C. Pérez-González, Y. Torres, F. Martín-Pedrosa, Electropolymerized polypyrrole silver nanocomposite coatings on porous Ti substrates with enhanced corrosion and antibacterial behavior for biomedical applications. Materials Today Chemistry, 29, (2023) 101433. https://doi.org/10.1016/j.mtchem.2023.101433

[30] N.A. Johari, J. Alias, A. Zanurin, N.S. Mohamed, N.A. Alang, M.Z.M. Zain, Recent progress of self-healing coatings for magnesium alloys protection. Journal of Coatings Technology and Research, 19(3), (2022) 757-774. https://doi.org/10.1007/s11998-021-00599-2

[31] L.Teo, V.R. Subramanian, D.T. Schwartz, Dynamic electrochemical impedance spectroscopy of lithium-ion batteries: Revealing underlying physics through efficient joint time-frequency modeling. Journal of the Electrochemical Society, 168(1), (2021) 010526. https://doi.org/10.1149/1945-7111/abda04

[32] A. Sharma, S. Sharma, Graphene-based polymer coatings for preventing marine corrosion: A review. Journal of Coatings Technology and Research, 20(2), (2023) 413-432. https://doi.org/10.1007/s11998-022-00730-x

[33] A. Rashidizadeh, H. Ghafuri, H.R. Esmaili Zand, N. Goodarzi, Graphitic carbon nitride nanosheets covalently functionalized with biocompatible vitamin B1: synthesis, characterization, and its superior performance for synthesis of quinoxalines. ACS omega, 4(7), (2019) 12544-12554. https://doi.org/10.1021/acsomega.9b01635

[34] S. Nagarajan, N. Rajendran, Crevice corrosion behaviour of superaustenitic stainless steels: dynamic electrochemical impedance spectroscopy and atomic force microscopy studies. Corrosion Science, 51(2), (2009) 217-224. https://doi.org/10.1016/j.corsci.2008.11.008

[35] S. Kang, Z. Fang, M. He, M. Chen, Y. Gao, D. Sun, Y. Liu, M. Chen, M. Dong, P. LiuCui, L. (2020). An instant, biocompatible and biodegradable high-performance graphitic carbon nitride. Journal of colloid and interface science, 563, 336-346. https://doi.org/10.1016/j.jcis.2019.12.021

[36] J. Marchi, V. Ussui, C.S. Delfino, A.H. Bressiani, M.M. Marques, Analysis in vitro of the cytotoxicity of potential implant materials. I: Zirconia-titania sintered ceramics. Journal of Biomedical Materials Research Part B: Applied Biomaterials, 94(2), (2010) 305-311. https://doi.org/10.1002/jbm.b.31652

[37] Y. Zhang, T. Cui, J. Zhao, Y. Yan, J. Jiang, Fabrication and study of a novel TiO2/g-C3N5 material and photocatalytic properties using methylene blue and tetracycline under visible light. Inorganic Chemistry Communications, 143, (2022)109815. https://doi.org/10.1016/j.inoche.2022.109815

[38] V. Patel, K. Ramadass, B. Morrison, J.S. John Britto, J.M. Lee, S. Mahasivam, P. Weerathunge, V. Bansal, J. Yi, G. Singh, A. Vinu, Utilising the Nanozymatic Activity of Copper-Functionalised Mesoporous C3N5 for Sensing Biomolecules. Chemistry–A European Journal, 29(69), (2023) e202302723. https://doi.org/10.1002/chem.202302723

[39] M. Subbiah, P. MuthuKrishnan, S. Venkatachalam, N. Srinivasan, A nanoporous mixed oxide coatings over 316L SS for orthopaedic implant applications. Journal of Bio- and Tribo-Corrosion, 7(3), (2021)113. https://doi.org/10.1007/s40735-021-00549-w

[40] J.H. Lee, H.S. Ryu, J.H. Seo, D.Y. Lee, B.S. Chang, C.K. Lee, Negative effect of rapidly resorbing properties of bioactive glass-ceramics as bone graft substitute in a rabbit lumbar fusion model. Clinics in Orthopedic Surgery, 6(1), (2014) 87-95. https://doi.org/10.4055/cios.2014.6.1.87

[41] B. Yilmaz, A.E. Pazarceviren, A. Tezcaner, Z. Evis, Historical development of simulated body

fluids used in biomedical applications: A review. Microchemical Journal, 155, (2020) 104713. https://doi.org/10.1016/j.microc.2020.104713

[42] Z.H.E.N. Zhen, T.F. Xi, Y.F. Zheng, A review on in vitro corrosion performance test of biodegradable metallic materials. Transactions of Nonferrous Metals Society of China, 23(8), (2013) 2283-2293. https://doi.org/10.1016/S1003-6326(13)62730-2

[43] T. Manoja, R. Abinaya, R. Anuradha, S. Nagarajan, Investigation and In Vitro Studies of a ZrO_2/g-C_3N_4 Composite Coated on 316L Stainless Steel for Biomedical Applications. Materials and Corrosion, (2024)1-11. https://doi.org/10.1002/maco.202414525

[44] J. Zhang, H. Tao, S. Wu, J.Y ang, M. Zhu, Enhanced durability of nitric oxide removal on TiO2 (P25) under visible light: Enabled by the direct Z-scheme mechanism and enhanced structure defects through coupling with C3N5. Applied Catalysis B: Environmental, 296, (2021) 120372. https://doi.org/10.1016/j.apcatb.2021.120372

[45] L. Lu, G. Wang, M. Zou, , Wang, J., & Li, J. Effects of calcining temperature on formation of hierarchical TiO2/g-C3N4 hybrids as an effective Z-scheme heterojunction photocatalyst. Applied Surface Science, 441, (2018) 1012-1023. https://doi.org/10.1016/j.apsusc.2018.02.080

[46] L. Cui, X. Ding, Y. Wang, H. Shi, L. Huang, Y. Zuo, S. Kang, Facile preparation of Z-scheme WO3/g-C3N4 composite photocatalyst with enhanced photocatalytic performance under visible light. Applied Surface Science, 391, (2017) 202-210. https://doi.org/10.1016/j.apsusc.2016.07.055

[47] M. Zarei, Ultrasonic-assisted preparation of ZrO2/g-C3N4 nanocomposites with high visible-light photocatalytic activity for degradation of 4-chlorophenol in water. Water-Energy Nexus, 3, (2020) 135-142. https://doi.org/10.1016/j.wen.2020.08.002

[48] X. He, D. Zhu, In situ solvothermal method of C 3 N 5@ NH 2-MIL-125 composites with enhanced visible-light photocatalytic performance. Journal of Materials Science: Materials in Electronics, (2021) 1-11. https://doi.org/10.1007/s10854-021-07308-0

[49] E.S. Andrés, M. Toledano-Luque, A.D. Prado, M.A. Navacerrada, I. Mártil, G. González-Díaz, W. Bohne, J. Röhrich, E. Strub, Physical properties of high pressure reactively sputtered TiO2. Journal of Vacuum Science & Technology A, 23(6), (2005) 1523-1530. https://doi.org/10.1116/1.2056554

[50] S. Gonuguntla, S. Sk, A. Tiwari, H. Mandal, P.N. Lakavath, V. Perupoga, U. Pal, Regulating surface structures for efficient electron transfer across h-BN/TiO2/gC3N4 photocatalyst for remarkably enhanced hydrogen evolution. Journal of Materials Science: Materials in Electronics, 32, (2021) 12191-12207. https://doi.org/10.1007/s10854-021-05848-z

[51] Y. Jiao, Y. Zhang, G. Zhang, M. Tian, J. Zhao, T. Cui, Y. Yan, J. Jiang, Formation of Z-scheme g-C3N5-BiOCl to enhance photocatalytic activity under visible light. Applied Organometallic Chemistry, 37(8), (2023) e7073. https://doi.org/10.1002/aoc.7073

[52] Y.O. Ibrahim, A. Hezam, T.F. Qahtan, A.H. Al-Aswad, M.A. Gondal, Q.A. Drmosh, Laser-Assisted Synthesis of Z-Scheme TiO_2/rGO/gC_3N_4 Nanocomposites for Highly Enhanced Photocatalytic Hydrogen Evolution. Applied Surface Science, 534, (2020) 147578. https://doi.org/10.1016/j.apsusc.2020.147578

[53] K.M. Lee, C.F. Kait, J.W. Lim, G.B. Teh, Raman Spectroscopy of TiO_2 Nanoparticles Synthesized by Hydrolysis of $TiCl_4$: Effect of Sulfate Ions Concentration. Proceedings of the 6th International Conference on Fundamental and Applied Sciences, (2021) 85–95. https://doi.org/10.1007/978-981-16-4513-6_8

[54] L. Kernazhitsky, V. Shymanovska, T. Gavrilko, V. Naumov, L. Fedorenko, V. Kshnyakin, J. Baran, Laser-excited excitonic luminescence of nanocrystalline TiO2 powder. Український фізичний журнал, 59(3), (2014) 248-255. https://doi.org/10.15407/ujpe59.03.0246

[55] J. Liu, S. Wang, C. Zhao, J. Zheng, Engineered g-C3N5-based nanomaterials for photocatalytic energy conversion and environmental remediation. Nanomaterials, 13(3), (2023) 499. https://doi.org/10.3390/nano13030499

[56] Z. Shahryari, M. Yeganeh, K. Gheisari, B. Ramezanzadeh, A brief review of the graphene oxide-based polymer nanocomposite coatings: preparation, characterization, and properties. Journal of Coatings Technology and Research, 18(4), (2021) 945-969. https://doi.org/10.1007/s11998-021-00488-8

[57] D. Pathote, D. Jaiswal, V. Singh, C.K. Behera, Electrochemical corrosion behavior of tantalum coated 316L stainless steel by DC Magnetron sputtering for orthopedic applications. Applied Surface Science Advances, 13, (2023) 100365. https://doi.org/10.1016/j.apsadv.2022.100365

[58] N.R. Vaidya, P. Aklujkar, A.R. Rao, Modification of natural gums for application as corrosion inhibitor: a review. Journal of Coatings Technology and Research, 19(1), (2022) 223-239. https://doi.org/10.1007/s11998-021-00510-z

[59] G.K. Ağçeli, H. Hammachi, S.P. Kodal, N. Cihangir, Z. Aksu, A novel approach to synthesize TiO_2 nanoparticles: biosynthesis by using Streptomyces sp. HC1. Journal of Inorganic and Organometallic Polymers and

Materials, 30, (2020) 3221-3229. https://doi.org/10.1007/s10904-020-01486-w

[60] X. Yuan, C. Zhou, Q. Jing, Q. Tang, Y. Mu, A. Du, Facile Synthesis of g-C_3N_4 Nanosheets/ZnO Nanocomposites with Enhanced Photocatalytic Activity in Reduction of Aqueous Chromium (VI) under Visible Light. Nanomaterials, 6(9), (2016) 173. https://doi.org/10.3390/nano6090173

[61] M. Oves, M.O. Ansari, R. Darwesh, A. Hussian, M.F. Alajmi, H.A. Qari, Synthesis and Antibacterial Aspects of Graphitic C_3N_4@Polyaniline Composites. Coatings, 10(10), (2020) 950. https://doi.org/10.3390/coatings10100950

[62] N. Khoshnood, M. Yeganeh, S.R.A. Zaree, A. Zamanian, An investigation on the biological and corrosion response of PEI coating on the AZ31 alloy. Journal of Coatings Technology and Research, 20(5), (2023) 1691-1701. https://doi.org/10.1007/s11998-023-00774-7

[63] A. Bashir, H. Siddiqui, S. Naseem, A.S. Bhatti, Ecofriendly water-based solution processing: preliminary studies of Zn-ZrO2 thin films for microelectronics applications. Coatings, 11(8), (2021) 901. https://doi.org/10.3390/coatings11080901

[64] Y. Gao, L. Wang, D. Li, The Surface Modification of ZrO2 Film by Zr/Nb Ion Implantation and First-Principles Calculation. Coatings, 13(10), (2023) 1696. https://doi.org/10.3390/coatings13101696

[65] M. Zhu, Q. Zhang, Y. Yuan, S. Guo, Y. Huang, Study on the correlation between passive film and AC corrosion behavior of 2507 super duplex stainless steel in simulated marine environment. Journal of Electroanalytical Chemistry, 864, (2020) 114072. https://doi.org/10.1016/j.jelechem.2020.114072

[66] P. Kumar, G. Anne, M.R. Ramesh, M. Doddamani, A. Prabhu, Enhancing the functionality of biodegradable Mg–Zn–Mn alloys using poly (lactic) acid (PLA) coating for temporary implants. Journal of Coatings Technology and Research, 21, (2024) 1525–1537. https://doi.org/10.1007/s11998-024-00913-8

[67] A.J. Nathanael, J.H. Lee, S.I. Hong, Effect of processing parameters on the mechanical reliability of ZrN/hydroxyapatite nanocomposite coatings. Advanced Science Letters, 15(1), (2012) 285-290. https://doi.org/10.1166/asl.2012.4177

[68] M.R. Noor El-Din, A.I. Hashem, R.E. Morsi, A. Abd El-Azeim, R.H. Mohamed, Facile fabrication of superhydrophobic nanocomposites coating materials using nanoemulsion polymerization technique and its application for protecting the petroleum carbon steel pipelines. Journal of Coatings Technology and Research, 20(1), (2023) 291-305. https://doi.org/10.1007/s11998-022-00669-z

[69] S. Jafari, M.M. Atabaki, J. Idris, Comparative study on bioactive coating of Ti-6Al-4V alloy and 316 L stainless steel. Association of Metallurgical Engineers of Serbia, 18(2), (2012) 145-158.

[70] S. Nagarajan, M. Mohana, P. Sudhagar, V. Raman, T. Nishimura, S. Kim, Y.S. Kang, N. Rajendran, Nanocomposite coatings on biomedical grade stainless steel for improved corrosion resistance and biocompatibility. ACS applied materials & interfaces, 4(10), (2012) 5134-5141. https://doi.org/10.1021/am301559r

[71] H.S. Klapper, J. Göllner, A. Heyn, A. Burkert, Relevance of the cathodic process on the passivation of stainless steels–an approximation to the origin of the rouging phenomenon. Materials and corrosion, 63(1), (2012) 54-58. https://doi.org/10.1002/maco.201005668

[72] D. Pathote, V. Singh, D. Jaiswal, R.K. Gautam, C.K. Behera, Improving the electrochemical corrosion behavior of stainless steel (316L) through the deposition of tantalum-based thin films. Materials Today: Proceedings, 112, (2024) 24-33. https://doi.org/10.1016/j.matpr.2023.08.003

[73] R. Manonmani, S. Mohandoss, S. Sureshkumar, Prevention of Corrosion on 316L Stainless Steel by Nano Biocomposite Coating for Bone Tissue Application. International Journal of Creative Research Thoughts (IJCRT), 11(3), (2023) 969-986.

[74] N. Yao, J. Chen, G. Zhao, Y. Huang, L. Yang, H. Li, Z. Sheng, UV irradiation grafting of acrylamide onto dopamine-modified 316L stainless steel. Journal of Coatings Technology and Research, 15, (2018) 1181-1189. https://doi.org/10.1007/s11998-018-0095-y

[75] H. Alias, J. Alias, N.A. Alang, Anticorrosion strategy for magnesium alloys through a superhydrophobic approach utilizing slippery liquid-infused porous surface coating. Journal of Coatings Technology and Research, (2024) 1-20. https://doi.org/10.1007/s11998-024-01003-5

[76] B. Diaz, L. Freire, M. Mojío, X.R. Nóvoa, Optimization of conversion coatings based on zinc phosphate on high strength steels, with enhanced barrier properties. Journal of Electroanalytical Chemistry, 737, (2015) 174-183. https://doi.org/10.1016/j.jelechem.2014.06.035

[77] Y. Sasikumar, A.M. Kumar, R.S. Babu, M.M. Rahman, L.M. Samyn, A.L.F. de Barros, Biocompatible hydrophilic brushite coatings on AZX310 and AM50 alloys for orthopaedic implants. Journal of Materials Science: Materials in Medicine, 29, (2018) 1-14. https://doi.org/10.1007/s10856-018-6131-8

[78] K. Kowalczyk, K. Przywecka, B. Grzmil, Influence

of novel ammonium-modified zinc-free phosphate nanofillers on anticorrosive features of primer-less polyurethane top-coating compositions. Journal of Coatings Technology and Research, 16, (2019) 401-414. https://doi.org/10.1007/s11998-018-0119-7

[79] Y. Cai, X. Quan, G. Li, N. Gao, Anticorrosion and scale behaviors of nanostructured ZrO2–TiO2 coatings in simulated geothermal water. Industrial & Engineering Chemistry Research, 55(44), (2016) 11480-11494. https://doi.org/10.1021/acs.iecr.6b02920

[80] M. Szociński, K. Darowicki, K. Schaefer, Application of impedance imaging to evaluation of organic coating degradation at a local scale. Journal of Coatings Technology and Research, 10, (2013) 65-72. https://doi.org/10.1007/s11998-012-9458-y

[81] S. Nagarajan, V. Raman, N. Rajendran, Evaluation of passive film behaviour of super austenitic stainless steels at different potential regions using dynamic electrochemical impedance spectroscopy. Journal of Solid State Electrochemistry, 14, (2010) 1197-1204. https://doi.org/10.1007/s10008-009-0948-5

[82] P. Dhaiveegan, N. Elangovan, T. Nishimura, N. Rajendran, Corrosion behavior of 316L and 304 stainless steels exposed to industrial-marine-urban environment: field study. RSC Advances, 6(53), (2016) 47314-47324. https://doi.org/10.1039/C6RA04015B

[83] L. Floroian, F. Sima, M. Florescu, M. Badea, A.C. Popescu, N. Serban, I.N. Mihailescu, Double layered nanostructured composite coatings with bioactive silicate glass and polymethylmetacrylate for biomimetic implant applications. Journal of Electroanalytical Chemistry, 648(2), (2010) 111-118. https://doi.org/10.1016/j.jelechem.2010.08.005

[84] D. Xia, Y. Ji, Y. Mao, C. Deng, Y. Zhu, W. Hu, Localized corrosion mechanism of 2024 aluminum alloy in a simulated dynamic seawater/air interface. Acta Metallurgica Sinica, 59(2), (2022) 297-308.

[85] H. Gerengi, S. Lorenzi, M.M. Solomon, P. Slepski, S. Gratton, M. Cabrini, A Probe into the Corrosion Behavior of a WE43B Magnesium Alloy in a Simulated Body Fluid using Dynamic Electrochemical Impedance Spectroscopy. Journal of Materials Engineering and Performance, (2023)1-11. https://doi.org/10.1007/s11665-023-09015-9

[86] M. Yousefpour, A. Afshar, X. Yang, X. Li, B. Yang, Y. Wu, J. Chen, X. Zhang, Nano-crystalline growth of electrochemically deposited apatite coating on pure titanium. Journal of Electroanalytical Chemistry, 589(1), (2006) 96-105. https://doi.org/10.1016/j.jelechem.2006.01.020

[87] M.U. Joshi, S.P. Kulkarni, M. Choppadandi, M. Keerthana, G. Kapusetti, Current state of art smart coatings for orthopedic implants: A comprehensive review. Smart Materials in Medicine, 4, (2023) 661-679. https://doi.org/10.1016/j.smaim.2023.06.005

[88] R. Ahmadi, A. Afshar, In vitro study: Bond strength, electrochemical and biocompatibility evaluations of TiO2/Al2O3 reinforced hydroxyapatite sol–gel coatings on 316L SS. Surface and Coatings Technology, 405, (2021) 126594. https://doi.org/10.1016/j.surfcoat.2020.126594

[89] M. Karthega, S. Nagarajan, N. Rajendran, In vitro studies of hydrogen peroxide treated titanium for biomedical applications. Electrochimica Acta, 55(6), (2010) 2201-2209. https://doi.org/10.1016/j.electacta.2009.11.057

[90] K.K. Amirtharaj Mosas, A.R. Chandrasekar, A. Dasan, A. Pakseresht, D. Galusek, Recent advancements in materials and coatings for biomedical implants. Gels, 8(5), (2022) 323. https://doi.org/10.3390/gels8050323

[91] S.M. Londoño-Restrepo, L.F. Zubieta-Otero, R. Jeronimo-Cruz, M.A. Mondragon, M.E. Rodriguez-García, Effect of the crystal size on the infrared and Raman spectra of bio hydroxyapatite of human, bovine, and porcine bones. Journal of Raman Spectroscopy, 50(8), (2019) 1120-1129. https://doi.org/10.1002/jrs.5614

[92] T.G.M. Bonadio, F. Sato, A.N. Medina, W.R. Weinand, M.L. Baesso, W.M. Lima, Bioactivity and structural properties of nanostructured bulk composites containing Nb2O5 and natural hydroxyapatite. Journal of Applied Physics, 113(22), (2013) 223505. https://doi.org/10.1063/1.4809653

[93] A. Salam, L. Lucia, H. Jameel, Starch derivatives that contribute significantly to the bonding and antibacterial character of recycled fibers. ACS omega, 3(5), (2018) 5260-5265. https://doi.org/10.1021/acsomega.8b00307

[94] M. Yunusa, X. Shu, S. Guan, Y. Liu, M. Ge, J. Wu, S. Yang, Osteogenic potential of polyacrylonitrile and multiwalled carbon nanotube composite coated on anodised titanium alloy for orthopedic applications. Polymer Bulletin, 79, (2022) 3147–3161. https://doi.org/10.1021/acsomega.8b00307

Authors Contribution Statement

Padma Santhiya Muthu Krishnan-Investigation, Methodology, Formal analysis, Writing - Original draft. Manoja Tharmaraj- Validation, Investigation. Abinaya Radhakrishnan- Validation, Investigation. Anuradha Ramani- Validation, Investigation. Nagarajan Srinivasan-Writing - Review & Editing, Visualization,

Supervision. All the authors read and approved the final version of the manuscript.

Funding

The author, Srinivasan Nagarajan, acknowledges the Tamil Nadu State Government Higher Education (H_2) Department is gratefully acknowledged for the establishment of the Central Instrument Facility (GO (Ms) No. I59) and DST-FIST Project (SR/FST/CSI – 247/2012) for their infrastructure support.

Competing Interests

The authors declare that there are no conflicts of interest regarding the publication of this manuscript.

Data Availability

The data supporting the findings of this study can be obtained from the corresponding author upon reasonable request.

Has this article screened for similarity?

Yes